



# Microstructure and Mechanical Properties of AlSi10Mg Alloy Manufactured by Laser Powder Bed Fusion Under Nitrogen and Argon Atmosphere

Yunmian Xiao<sup>1</sup> · Yongqiang Yang<sup>1</sup> · Shibiao Wu<sup>1</sup> · Jie Chen<sup>1</sup> · Di Wang<sup>1</sup> · Changhui Song<sup>1</sup>

Received: 20 July 2021 / Revised: 11 September 2021 / Accepted: 1 October 2021 / Published online: 27 November 2021  
© The Chinese Society for Metals (CSM) and Springer-Verlag GmbH Germany, part of Springer Nature 2021

## Abstract

In order to study the effect of gas atmosphere on forming performance of laser powder bed fusion (LPBF), AlSi10Mg alloy was prepared by direct forming and in situ laser remelting under the shielding gas of argon and nitrogen in this study, and its microstructure and properties were characterized and tested, respectively. The results show that the forming performance of AlSi10Mg under nitrogen atmosphere is better than that of argon. Moreover, in situ laser remelting method can effectively enhance the relative density and mechanical properties of AlSi10Mg, in which the densification is increased to 99.5%. In terms of mechanical properties, after in situ remelting, ultimate tensile strength under argon protection increased from  $444.85 \pm 8.73$  to  $489.45 \pm 3.20$  MPa, and that under nitrogen protection increased from  $459.21 \pm 13.77$  to  $500.14 \pm 5.15$  MPa. In addition, the elongation is nearly doubled and the micro-Vickers hardness is increased by 20%. The research results provide a new regulation control method for the customization of AlSi10Mg properties fabricated by LPBF.

**Keywords** In situ laser remelting · Laser powder bed fusion · AlSi10Mg alloy · Mechanical properties · Shielding gas

## 1 Introduction

Aluminum alloy has lightweight, high thermal conductivity and good mechanical properties [1]. It is widely used in aerospace, automobile and traditional manufacturing industries [2]. However, traditional manufacturing methods, such as casting, are prone to produce pore inclusions, resulting in poor performance of parts. Forging requires expensive and complex molds, which increases production costs and lead times [3]. Therefore, there is an urgent need for a technology suitable for producing complex parts in small batches and short delivery time. Laser powder bed fusion (LPBF) is one of the most promising metal additive manufacturing (AM) techniques, which provides unique and great potential for manufacturing parts with complex geometry. These features make it meet the requirements mentioned earlier, while selective laser melting (SLM) based on laser

beam high-speed scanning (maximum speed 7 m/s) is currently one of the most widely used LPBF technologies. It selectively melts the pre-laid thin layer powder to manufacture bulk parts layer by layer. One considerable advantage of SLM is that processing thin powder layer (usually 20–100  $\mu\text{m}$ ) on the substrate with small laser spot diameter (about 70  $\mu\text{m}$ ) can accelerate the cooling rate of metal powder melting and solidification ( $10^6$ – $10^8$   $^\circ\text{C/s}$ ) [4]. For this reason, SLMed metallic materials were known to produce unique microstructures, such as melt pools and fine grain structures. Another advantage of SLM is that slicing based on the 3D model can easily manufacture parts with complex geometric structures, such as implicit curved porous radiator.

SLM forming process is affected by plenty of parameters. During the SLM processing of AlSi10Mg, the molten pool is extremely unstable with obvious spark spatter, which is easy to form pores, indicating an evident need to reduce porosity [5]. And from printing parameters such as laser power or scanning speed to post-treatment processes such as heat treatment, these process parameters determine the final mechanical properties of parts. Since pores and cavities will weaken the structure of parts, it is an effective method to improve the relative density of manufactured parts in order to obtain the best mechanical properties [6]. Scanning

Available online at <http://link.springer.com/journal/40195>.

✉ Changhui Song  
song\_changhui@163.com

<sup>1</sup> School of Mechanical and Automotive Engineering, South China University of Technology, Guangzhou 510640, China

strategy is one of significant parameters affecting porosity, microstructure orientation and crack formation. SLM processing parameters (laser power, scan speed, hatch spacing, and block size) affect the porosity and mechanical microstructure of AlSi10Mg [7, 8]. The results showed that local cracking was caused by a large amount of unmelted powder, which warns that it was of great significance to optimize the laser processing parameters. Coincidentally, Thijs et al. [9] also investigated the effects of unidirectional scanning and bidirectional scanning on the pre-alloyed AlSi10Mg. The hardness of AlSi10Mg alloy processed by SLM in their study was only  $127 \pm 3$  HV0.5; however, Thijs et al. [9] found that rotating the scanning direction within or between layers by  $90^\circ$  can improve some characteristics, such as microstructure homogeneity or surface quality. However, rotating the scanning direction within or between layers by  $90^\circ$  can improve some characteristics, such as microstructure homogeneity or surface quality.

Meanwhile, the researchers studied the effects of different process parameters on the porosity and surface roughness of 316 stainless steel, Ti6Al4V [10] and 18Ni300 [11] were studied. The results showed that the remelting scanning strategy was effective in reducing porosity and increasing part density, but at the cost of increasing production time. Specifically, the appropriate remelting parameters can reduce the average surface roughness to approximately Ra 4  $\mu\text{m}$ . Selective remelting of the final layer may also be advantageous in improving surface finish. It was also found that laser surface remelting (LSR) would affect the chemical properties of Ti6Al4V parts prepared by SLM. The thickness of the surface oxide layer of laser surface remelting sample was twice that of the non-surface remelted [12]. Although some people have studied the laser remelting of titanium alloy and stainless steel, few pay attention to the effect of the in situ laser remelting on AlSi10Mg with higher laser reflectivity. Besides, the mechanical properties of AlSi10Mg alloy obtained by previous SLM are generally lower than 450 MPa, which is far from meeting the requirements of aerospace and automotive parts. Therefore, in order to manufacture high-performance aluminum alloy parts, it is necessary to further study the effect mechanism of in situ laser remelting on microstructure and tensile properties of AlSi10Mg alloy.

In addition, shielding gas plays an important role in the quality of selective laser melting (SLM) parts by protecting metals from high-temperature oxidation. In terms of the influence of inert shielding gas atmosphere (Ar, N<sub>2</sub> or He) on laser powder bed fusion, a comparative study of SLM manufacturing under argon and helium atmospheres was carried out to better understand the impact of gas atmosphere on the process stability, and the nickel base alloy and single melt channel structure were investigated [13]. The results show that no matter what kind of shielding gas used, the influence

for the size of the single track presented to be constant, and the spatters generated fewer and smaller with the increase in the volume energy density under helium atmosphere. The atmosphere used either Ar or N<sub>2</sub> has not minutely stated for the AlSi10Mg alloys processed by SLM [14].

In this study, the SLM process has been combined with in situ laser remelting to manufacture the AlSi10Mg alloy. The main focus of this work is to study the effect of the in situ laser remelting on the microstructure and the mechanical properties. The in situ remelting was also implemented to further reduce porosity and spatter. Furthermore, we correlate the influence of the in situ laser remelting heat treatment input with the microstructures (such as phase formation, melt pool), the Vickers microhardness and mechanical properties. Meanwhile, the texture and tensile properties of AlSi10Mg alloy fabricated by SLM under different inert gas (nitrogen or argon) are wholly considered.

## 2 Experimental

### 2.1 Materials and LPBF Equipment

The powder used in the experiment was a gas-atomized AlSi10Mg alloy (AVIMETAL AM Co., Ltd., China). Figure 1a shows scanning electron microscopy (SEM) micrographs of the powder morphology, and illustration displays nearly spherical in shape of the powder. Figure 1b shows the particle size distribution of AlSi10Mg powder, which measured by HORIBA LA960S type laser particle size analyzer. The particle size of the used AlSi10Mg powder was 53–105  $\mu\text{m}$  with excellent flowability [15] of 42 s/50 g obtained by Hall flowmeters in accordance with the ASTM B213-17 standard [16]. Table 1 provides the chemical composition of the used AlSi10Mg alloy powder comparing with the ISO 3522 standard [17]. This study was conducted in a DiMetal-100 LPBF equipment (South China University of Technology, China), and Fig. 2a illustrates its technical principles in this study. It consists of an IPG's 500 W Ytterbium fiber laser (1070 nm wavelength), a high-precision scanning galvanometer at maximum speed of 7000 mm/s. The thickness of the processing layer is within 20–100  $\mu\text{m}$ , and the largest forming size of the parts is 100 mm  $\times$  100 mm  $\times$  150 mm. High purity nitrogen or argon was imported during the building process to exhaust oxygen.

### 2.2 Selective Laser Melting Process

Figure 2b shows the principle of S-cross orthogonal inter-layer stagger scanning strategy adopted in the additive manufacturing process of the AlSi10Mg alloy. Scanning line is half staggered from the two scanning distances of the previous scanning layer, and the X–Y scanning path

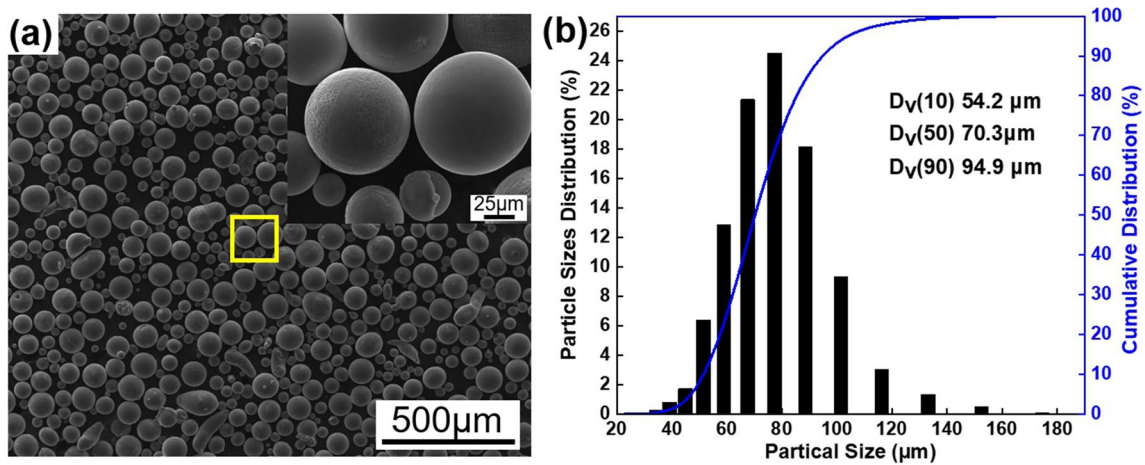


**Fig. 1** **a** SEM images of AlSi10Mg powder, **b** particle size distribution of AlSi10Mg powder used

**Table 1** Chemical composition of the used AlSi10Mg alloy powder and ISO 3522 standard AlSi10Mg powder (wt%)

Powder	Al	Si	Mg	Fe	Mn	Zn	Others
AlSi10Mg	Bal	10.15	0.35	0.16	0.20	0.043	<0.10
ISO 3522 [17]	Bal	9–11	0.20–0.45	<0.55	<0.45	<0.1	–

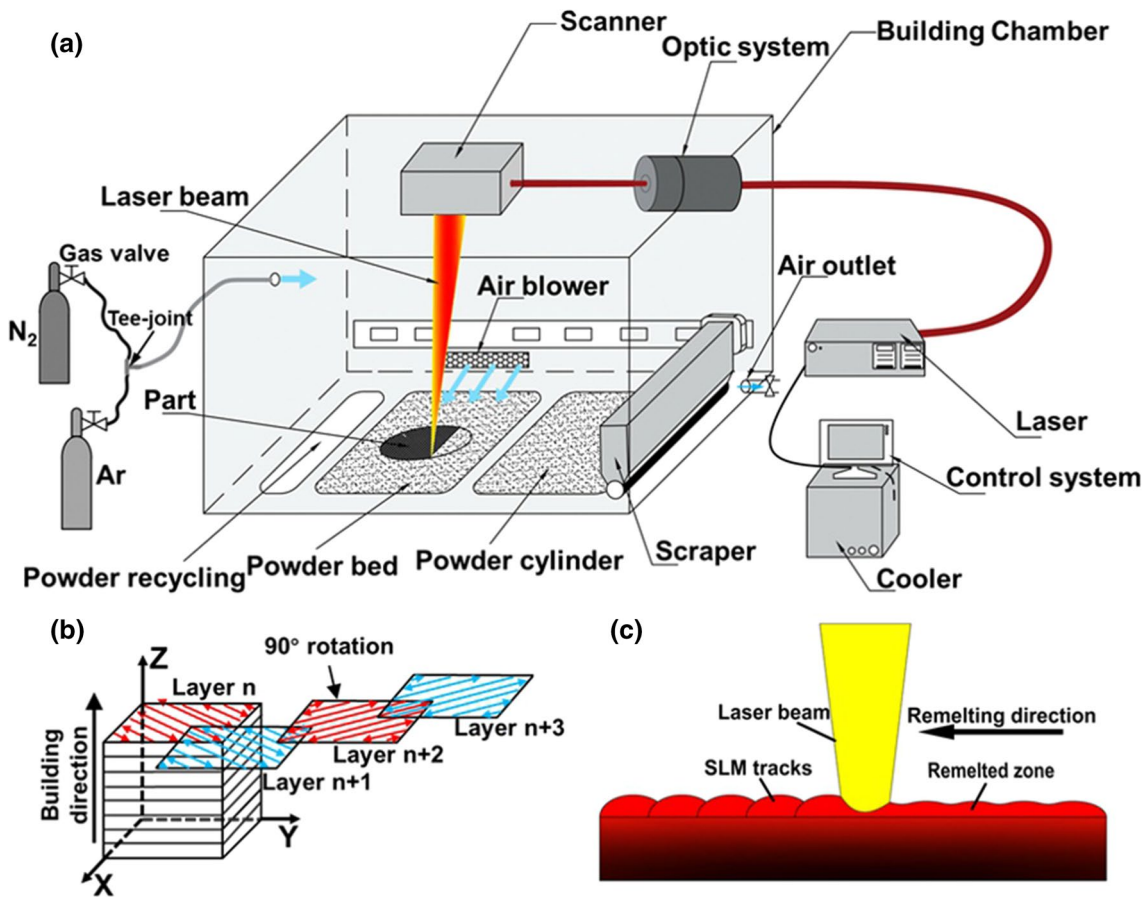


**Fig. 2** **a** Schematic of the experimental SLM equipment, **b** scanning strategy of “S-cross Orthogonal inter-layer stagger,” **c** schematic diagram of SLM remelting process

is in the shape of "S." The laser remelting scanning was rotated 90° from the starting direction of the previous layer. The SLM process in this study based on the optimized processing parameters already performed [18], as in detail listed in Table 2. Our optimized parameters were using a laser power of 220 W, a scanning speed of 1100 mm/s, a hatching space of 80  $\mu\text{m}$  and layer thickness of 30  $\mu\text{m}$ . In case of laser remelting, a laser power of 200 W, scanning speed of 1200 mm/s and hatching space of 80  $\mu\text{m}$  were used. Figure 2c presents a schematic diagram of SLM remelting process, and the parts were scanned again immediately without recoating powder after selective laser scanning a layer and melting the AlSi10Mg powder.

The sample manufacturing process consists of four steps and formed parts as shown in Fig. 3a. Firstly, the SLRM-Ar samples of AlSi10Mg alloy were printed on the aluminum substrate under a high purity argon atmosphere. Then, once the specimens' building height reached 8 mm, the build processing was interrupted and open the door of the building chamber to allow air to fully flooded. After this step, the building chamber was purged with high purity nitrogen until the oxygen level below 100 ppm, then keeping building SLM remelting samples (SLRM-N<sub>2</sub>) with the same height as the previous step constructed. To be clear, SLMed samples were constructed in a nitrogen atmosphere (SLM-N<sub>2</sub>) and argon atmosphere (SLM-Ar) in turn. During the whole manufacturing process, the

chamber oxygen content controlled within 100 ppm and the pressure was held at 20–40 mbar.

### 2.3 Microstructure Characterization

Samples were cut off from the building Al-based substrate by wire electrical discharge machining using water-based coolant and subsequently cleaned of oil by ultrasonic cleaning. Prior to performing any metallography, phase identification of as-built samples was conducted by X-ray diffraction (PANalytical X'pert Powder, Netherlands) with Cu K $\alpha$  radiation at 40 kV and 40 mA, using a continuous scan mode and scanning range of 20°–100° at scan step size of 0.013°. Four 8 mm  $\times$  8 mm  $\times$  8 mm cubical samples' density (theoretical density in this work: 2.68 g/cm<sup>3</sup>) measurements were performed using distilled water by Archimedes method [19]. After the sample was cut off from the substrate, it was mechanically polished with SiC paper (#400, #800, #1200, #2000 grit size), and then final surface polishing with a 0.05  $\mu\text{m}$  silica suspension by an automatic metallographic grinding and polishing machine. Subsequently, samples were etched with Keller's reagent (2.5 mL HNO<sub>3</sub>, 1.5 mL HCl, 1 mL HF, and 95 mL distilled water) for 40 s and cleaned with alcohol. The microstructure, scanning tracks, and molten pools were investigated by using an optical microscope (LEICA DMI 5000 M, Germany). The quantitative image analysis of grain size was carried out based on SEM images using traditional line interception technique [20] by ImageJ software. For each specific process, data

**Table 2** SLM processing parameters used for four batches of AlSi10Mg alloy

	Laser power (W)	Scanning speed (mm/s)	Scanning space ( $\mu\text{m}$ )	Layer thickness ( $\mu\text{m}$ )	Atmosphere
SLM	220	1100	80	30	Argon or nitrogen
SLM remelting	200	1200	80	–	Argon or nitrogen

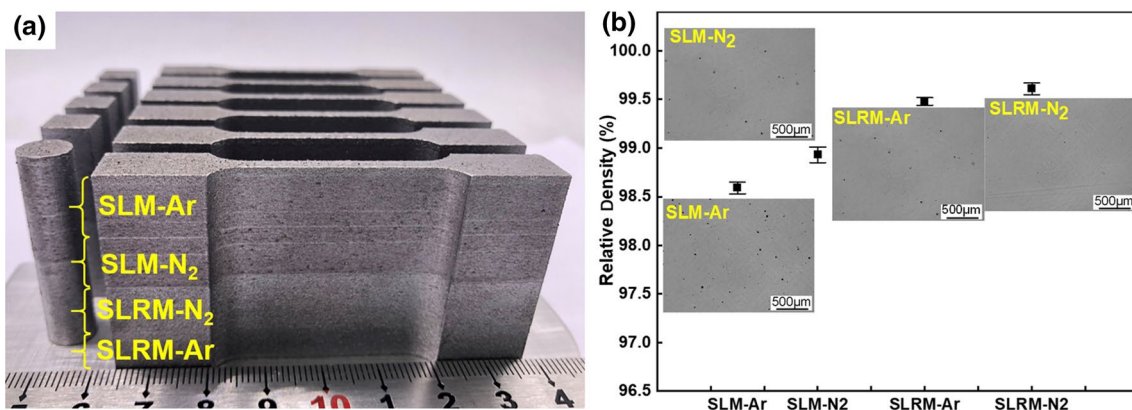


**Fig. 3** **a** Bulk and tensile test samples (8 mm height for each items) fabricated by SLRM-Ar, SLRM-N<sub>2</sub>, SLM-N<sub>2</sub> and SLM-Ar in turn, **b** relative density of SLM and SLRM parts



were obtained from three SEM images. Microstructure and fracture morphology were analyzed by scanning electron microscopy (NOVA NanoSEM 430 and QUANTA 200, Netherlands); in addition, the chemical composition of the manufactured parts was analyzed with electron-dispersive spectroscopy (EDS).

## 2.4 Mechanical Properties

Tensile samples were fabricated using optimized process parameters with cross section and gage length of 3 mm × 3 mm and 25 mm, respectively, which according to the ISO 6892-1:2019 standard [21] as shown in Fig. 3a. After tensile samples were cut from the substrate, the tensile tests were performed on an electronic universal testing machine (CMT5105, China) with 100 kN maximum force and an electronic extensometer. Six specimens were used for each group for the purpose of ensuring the data reliability. Tensile specimens were deformed to displacement control at 0.2 mm/min at room temperature. In addition, the Vickers microhardness measurements were carried out on the polished sample by HVS-1000Z microhardness tester under a load of 200 g (1.96 N) and a loading time of 15 s. A total of 10 points were measured on the side of each batch of samples with an interval of 0.5 mm along the building direction.

## 3 Results and Discussion

### 3.1 Phase Identification and Composition

X-ray diffraction analysis (XRD) was performed on the samples' surface to do the phase composition analysis.

The XRD test results of AlSi10Mg alloy samples with different SLM scanning strategies are shown in Fig. 4. Obviously, the peaks of SLRM-Ar/SLRM-N<sub>2</sub> samples were similar to the ones of the SLM-Ar/SLM-N<sub>2</sub> sample, which means that the phase composition in all samples is similar. Besides, it can be seen from Fig. 4a that all AlSi10Mg alloy samples formed by SLM consist of the diffraction peaks of  $\alpha$ -Al phase and Si phase. Particularly, the SLMed AlSi10Mg samples prepared by in situ remelting show obvious crystallographic texture growth along the (1 1 1) plane. Compared with the standard powder at 38.472° (from ICDD card 04-0787), the main peak ( $2\theta$ ) of Al (1 1 1) of the SLMed alloy moved to right as shown in Fig. 4b. The diffraction peak of SLRM-Ar sample was 38.5013° comparing with the SLM-Ar of 38.5041°. This is because the rapid solidification of the melt pool makes the silicon and magnesium in the  $\alpha$ -Al matrix present a supersaturated and solid solution. According to the Bragg's law [22],  $2d \sin \theta = n\lambda$  ( $n = 1, 2, 3, \dots$ ), the larger  $2\theta$  values indicated the smaller lattice constant, which means that the non-equilibrium metallurgical process induced by the laser causes the distortion of the aluminum matrix lattice. Lattice distortion leads to grain refinement due to the remelting scanning strategy in Al-7Si parts produced by laser remelting [23]. In addition, the effect of thermal stress caused by high-temperature gradient of remelting cannot be ignored [24]. In SLM process, the lower deposited layer is continuously subjected to the heat conduction cycle of the upper surface layer, which is equivalent to artificial aging treatment. During the in situ laser remelting heat treatment, Si precipitates and dissolves in the  $\alpha$ -Al matrix, resulting in lattice distortion. Similar changes were observed in nitrogen atmosphere as well.

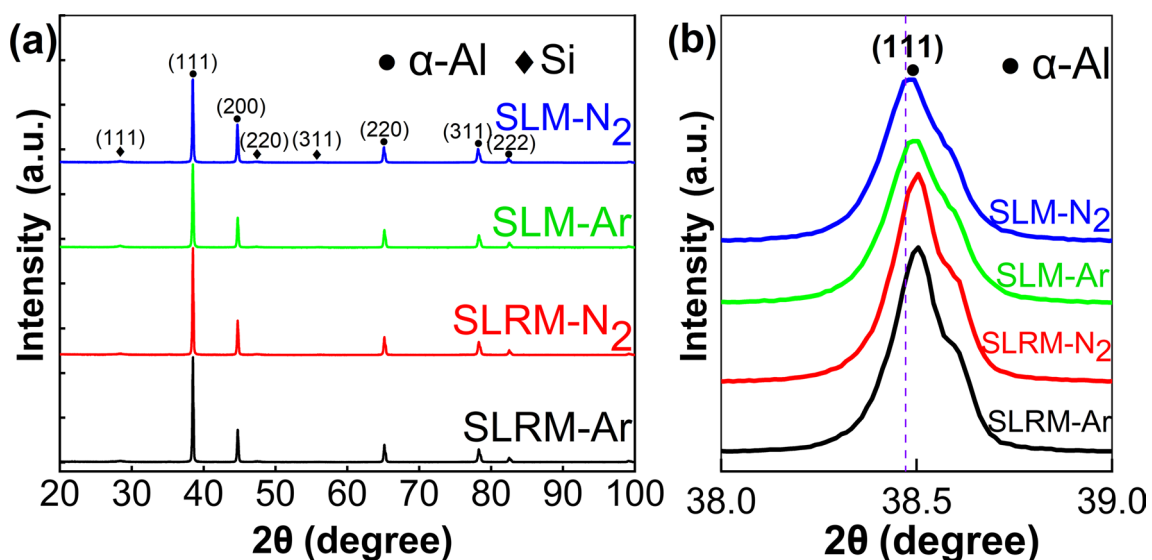


Fig. 4 **a** XRD patterns of AlSi10Mg SLM and SLRM samples in argon/nitrogen atmosphere, **b** small range of  $2\theta$  (38°–39°)

Moreover, a good bonding primarily decides the performance of the entire part. Figure 3b shows the relative density of as-built AlSi10Mg cubic samples, and illustrations are the microstructural image obtained by an optical microscope (OM). Compared with the SLMed AlSi10Mg samples, the remelted parts showed better density performance. The relative density of AlSi10Mg fabricated by SLM-Ar and SLM-N<sub>2</sub> was only  $98.59\% \pm 0.06\%$  and  $98.93\% \pm 0.08\%$  with large size pores. This may be caused by the high laser reflectivity and thermal conductivity of coarse AlSi10Mg powder. In addition, lack of fusion powder can easily lead to pores between the interlayers [25]. However, the SLRM-Ar and SLRM-N<sub>2</sub> specimens without visible pores possessed the highest relative density of  $99.48\% \pm 0.02\%$  and  $99.61\% \pm 0.06\%$ , respectively. Therefore, the in situ laser remelting could significantly enhance the density of parts.

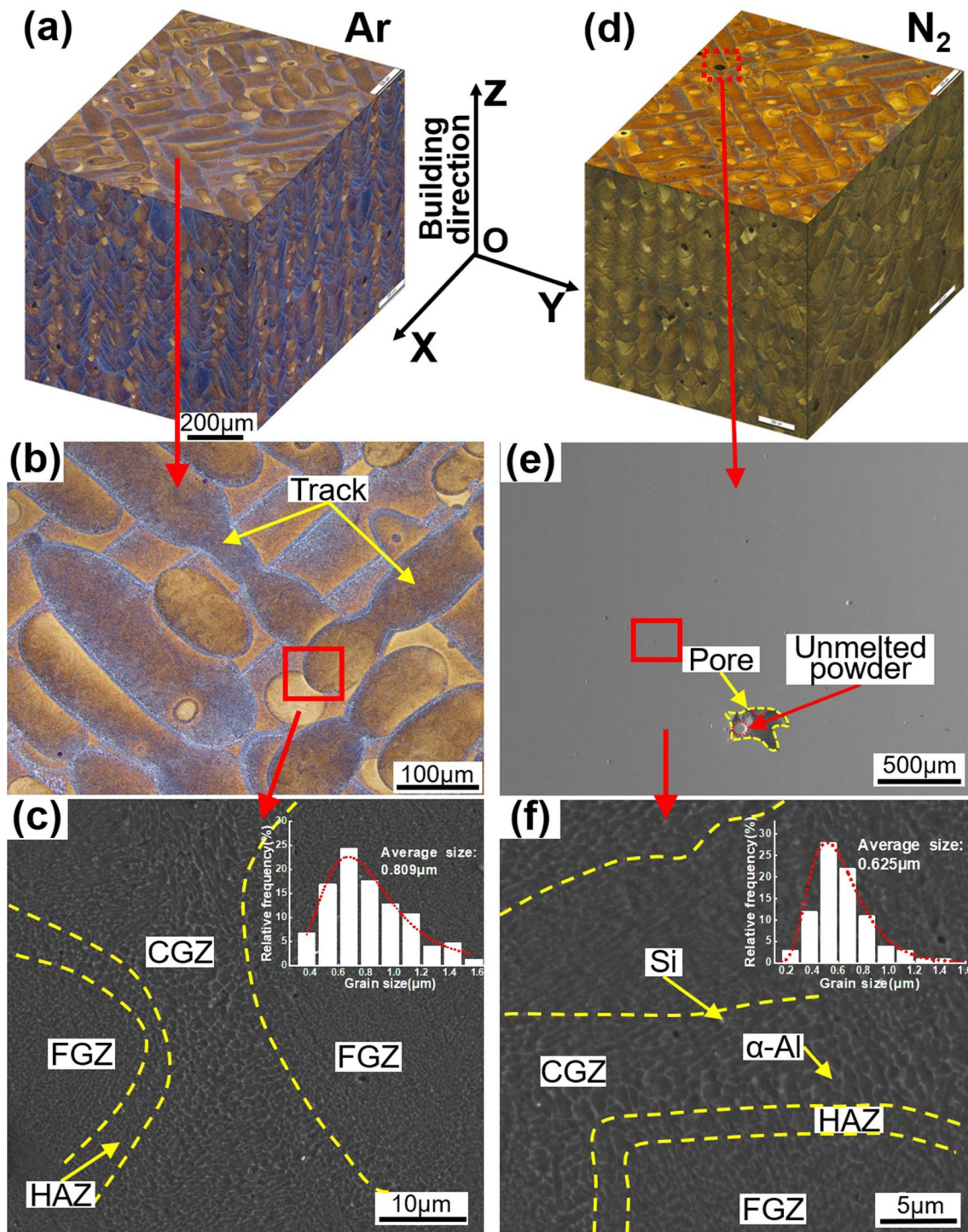
### 3.2 Microstructure of SLMed and SLRMed Samples

Figure 5 shows the microstructure and morphology of SLMed samples. In Fig. 5a, d, typical laser tracks can be noticed on the top (XOY) surface with S-cross Orthogonal inter-layer strategy, and elliptical shape between the molten pools can be observed clearly in the front (YOZ) and side (XOZ) views, as well as some holes, including the lack of melted voids (Fig. 5e) and gas pores [26] existed in the melt pool. The profile of scanning tracks reveals that the microstructure of materials produced by the SLM was rather inhomogeneous, as shown in Fig. 5b, which represented single welding track and solidified grain boundaries. Along the scanning tracks, it presented equiaxed cells whereas columnar obviously along with the molten pools. There were metallurgical pores in the microstructure that occurred along solidification grain boundaries, locally exceeding the fusion boundary without cracks. Two main phases existed in the AlSi10Mg alloy processed by SLM: one was a white network phase, and the other was a gray island phase. White phases distributed in a continuous network are the eutectic Si phase, and the gray phases with small islands are the  $\alpha$ -Al phase [27, 28]. Grains of the AlSi10Mg alloy fabricated by SLM were very fine with many grain boundaries (see Fig. 5c, f), compared with cast Al-Si alloys [29], which slightness-needle silicon particles precipitated in the soft  $\alpha$ -Al phase. This indicates that the solubility of silicon in the soft  $\alpha$ -Al matrix is enhanced during the SLM process, as evidenced by XRD (Fig. 4b). The reason is that the solidification rate of the melt pool is very quick (generally up to  $10^6$ – $10^8$  °C/s). The  $\alpha$ -Al in the liquid phase preferentially nucleates and grows during the SLM manufacturing process, so that the Si components in the liquid phase are discharged to the front of the solid–liquid interface, leading to an increase for enrichment of Si atoms in the remaining liquid phase [30]. Moreover, the solution reaches eutectic

composition, forming a [ $\alpha$ -Al + Si] co-crystal structure distributed in the grain boundary of  $\alpha$ -Al phase, which generates a continuous fine grains network structure.

Three distinct areas can be distinguished at the boundary of the molten pool (Fig. 5c, f): the fine-grained zone (FGZ), the coarse-grained zone (CGZ), and the heat-affected zone (HAZ). These are generally considered to be caused by different solidification rates due to the thermal gradient along the molten pool [31]. Since the crystallized solid phase with lower temperature had an effect of absorbing and dissipating heat, a large degree of supercooling occurred in the thin liquid layer after remelting in the region close to the crystallized solid phase. Therefore, a large amount of crystal nuclei will be produced in the thin liquid layer and the adjacent crystal nucleus quickly meet each other during the growth process, and unable to continue to grow, resulting in forming a fine-grained zone (Fig. 5f). The CGZ is located in the center of the remelted zone formed by the adjacent laser melting of AlSi10Mg alloy powder. Compared with the FGZ, the coarse-grained region owning a thicker cell wall indicates that the grains in this region re-nucleate and grow during the short period cooling process after laser remelting and maybe occurred the segregation of Si reinforced phase [32]. Another factor is that the CGZ was the farthest away from both sides (the unmelted powder region and the crystallized solid phase region) with the worst heat dissipation conditions, and rather serious heat accumulation as well. Compared with spontaneous nucleation, the solidification process of the remelted liquid was mainly the direct epitaxial growth based on columnar dendrites of some fine crystal regions close to the liquid phase as the substrate because of the lower Gibbs free energy requiring for direct growth from the crystallized solid phase, which led to coarsening of the crystal grains (Fig. 5c). The HAZ is located at the boundary of the remelting zone where the laser energy is insufficient to remelt the crystalline solid phase. It was formed by partial dissolution, fracture and nodulizing of the eutectic Si phase in the bottom layer with continuous network distribution under the effect of thermal cycle generated by heat input from the upper layer [33]. In the SLM process, heat treatment will be performed on the consolidated material due to the temperature is below the fusing point when the following layer is scanned. That will lead to element diffusion, and even the formation of hydrogen pores and heat-affected zones, which will significantly reduce the yield strength of the material. The width of the CGZ and the HAZ majorly depends on processing parameters such as laser power, scanning speed and hatch spacing [18, 34].

Figure 6 shows the microstructure of SLRM-processed samples under nitrogen or argon atmosphere. The molten pool boundaries induced Al–Si eutectic microstructure are clearly visible along the building direction by rapid solidification. Due to the remelting of the previously solidified



**Fig. 5** OM images of the SLM AISi10Mg alloys. Scanning track, molten pool morphology, and grain size details of the alloy from **a–c** SLM-Ar built, **d–f** SLM-N<sub>2</sub> built

bottom layer, the depth and shape of the molten pool are changed, which leads to the interruption of the scanning track of the single molten channel. Compared with the region without laser remelting, the laser remelted zone showed a finer dendrite microstructure. Rapid remelting

and resolidification can explain the uniform distribution and refinement of microstructure. Moreover, owing to good metallurgical fusion, the number of metallographic pores was lower and defects such as voids and inclusions were not found in the microstructure. The same results had been



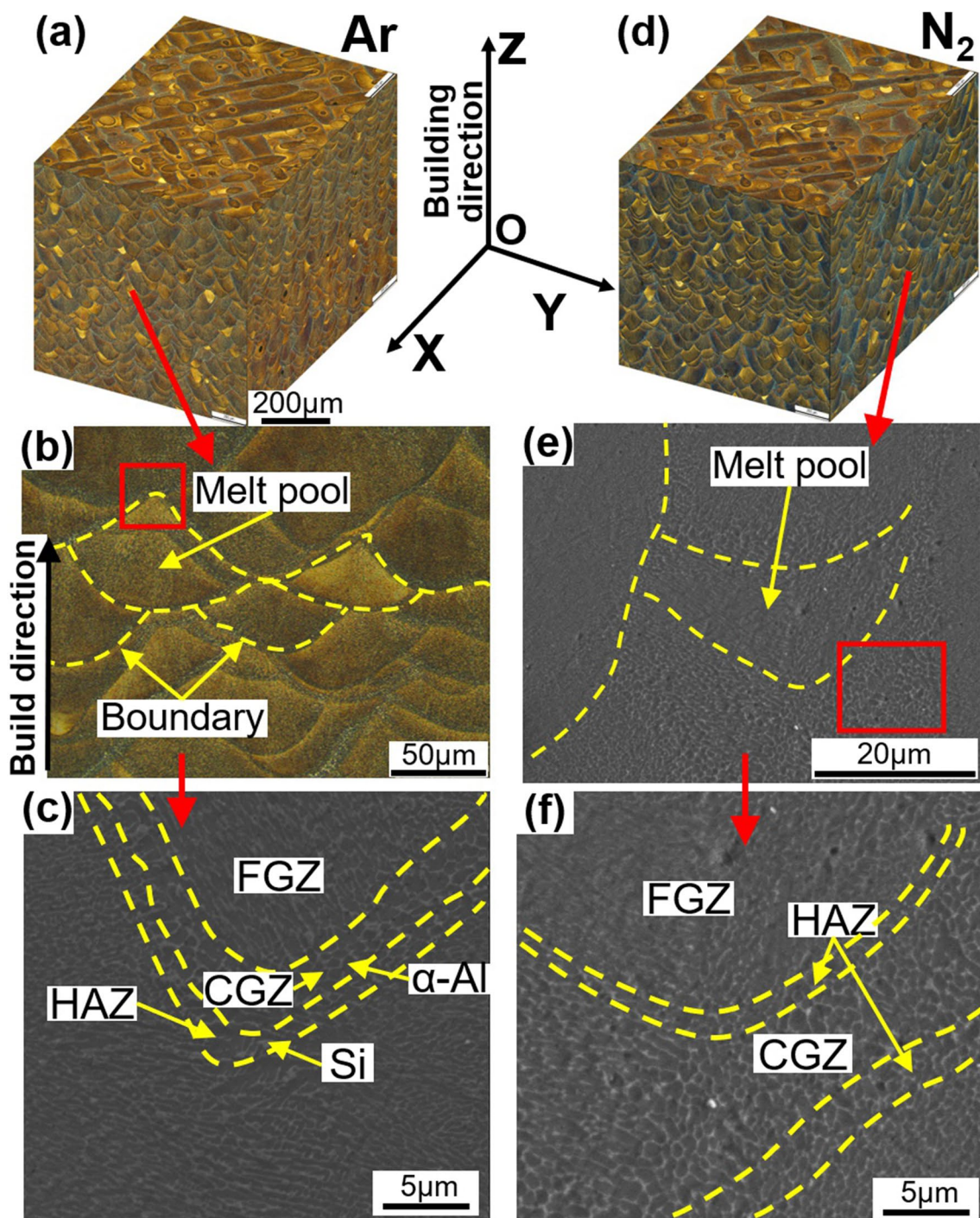


**Fig. 6** OM and SEM images of the SLMed AlSi10Mg alloys. Scanning track and molten pool morphology details of the alloy from **a–c** SLRM-Ar built, **d–f** SLRM-N<sub>2</sub> built

found in Cu–Al–Ni–Mn alloy manufactured by selective laser remelting [24]. Under the remelting strategy, many fine dendritic microstructures with different shapes and sizes are presented to the molten pool boundary. Thus, the  $\alpha$ -Al matrix presents a diamond-shaped distribution of molten pool. The size of the fine-grained structure and the

coarse-grained structure in the molten pool is about 0.35  $\mu\text{m}$  and 0.98  $\mu\text{m}$ , respectively, and there is a heat-affected zone (HAZ) around the molten pool. Demir and Previtali [11] showed that the grain structure of 18Ni300 maraging steel was refined after laser remelting, which obtained the upper fine grain structure and the lower coarse grain structure.



Therefore, it can be inferred that fine crystals are formed inside the molten pool, and then begin to coarsen near the center, until reaching the heat-affected zone at the boundary.

Figure 7 shows depth of molten pool and the distance between the previous layer and remelted layer. Obviously, the in situ laser remelting effectively reduced the depth of the molten pool, causing a significantly finer lamellar structure without clear crescent shape. The penetration depths  $H$  of SLM-Ar and SLM-N<sub>2</sub> parts are  $221 \pm 16 \mu\text{m}$  and  $245 \pm 26 \mu\text{m}$ , respectively. With the additional laser remelting, the distance  $h$  between layers of SLRM-N<sub>2</sub> is only  $37 \pm 6 \mu\text{m}$  to SLRM-Ar of  $42 \pm 9 \mu\text{m}$ . The reason is that the thermal conductivity and reflectivity of laser in the AlSi10Mg parts are higher than that of the powder, resulting in the laser incompletely remelt the molten pool of prior layer (Figs. 6, 7). Besides, due to the more quickly cooling rate in nitrogen atmosphere, the melt pool depth after remelting was shallower than that in argon atmosphere (Fig. 7c, d).

Figure 8a presents the growth refinement mechanism of eutectic Si in the SLM process. Under the laser thermal irradiation, the Si crystal melt, cracked and nodulized, and supersaturated Si was continuously precipitated. The two synergistic effects of needle-shaped and spheroids eutectic Si are uniformly distributed in the  $\alpha$ -Al matrix. Furthermore, the formation of Si dendrite microstructure is also influenced by the overall cooling rate in the SLM process. According to the long-standing solidification principle of metals and

alloys [35, 36], the solidification process of SLM in argon/nitrogen atmosphere can also be expressed in the following form:

$$R = G \cdot S \quad (1)$$

where  $R$  is the cooling rate,  $S$  is the solidification rate, and  $G$  is the thermal gradient. During the SLM process, the laser irradiation generated heat energy following a Gaussian distribution [37], and the cooling rate  $R$  inside the molten pool varied with the thermal gradient  $G$ . The mode of solidification and characteristic fineness depend on the ratio of thermal gradient  $G$  to solidification rate  $S$ . When the  $G/S$  ratio is less than the criterion of columnar to equiaxed transition, the transition will occur [38]. According to the gas thermal conductivity [39], the thermal conductivity of Nitrogen [0.0258 W/(mK)] is roughly 45% higher than Argon [0.0178 W/(mK)] range from 800 to 2000 K. Therefore, the laser remelting scanning cracking silicon phase moves farther under nitrogen atmosphere than in argon, and the recrystallization nucleation rate is more quickly, resulting in finer crystalline microstructures, as shown in Fig. 8b, c. Porous and unfused powder particles are also largely eliminated, further providing good metallurgical bonding and performance.

EDS analysis (Fig. 9) shows that most of the Si were concentrated on the grain boundary, and the remaining small part of Si was distributed in the crystal grains. This also

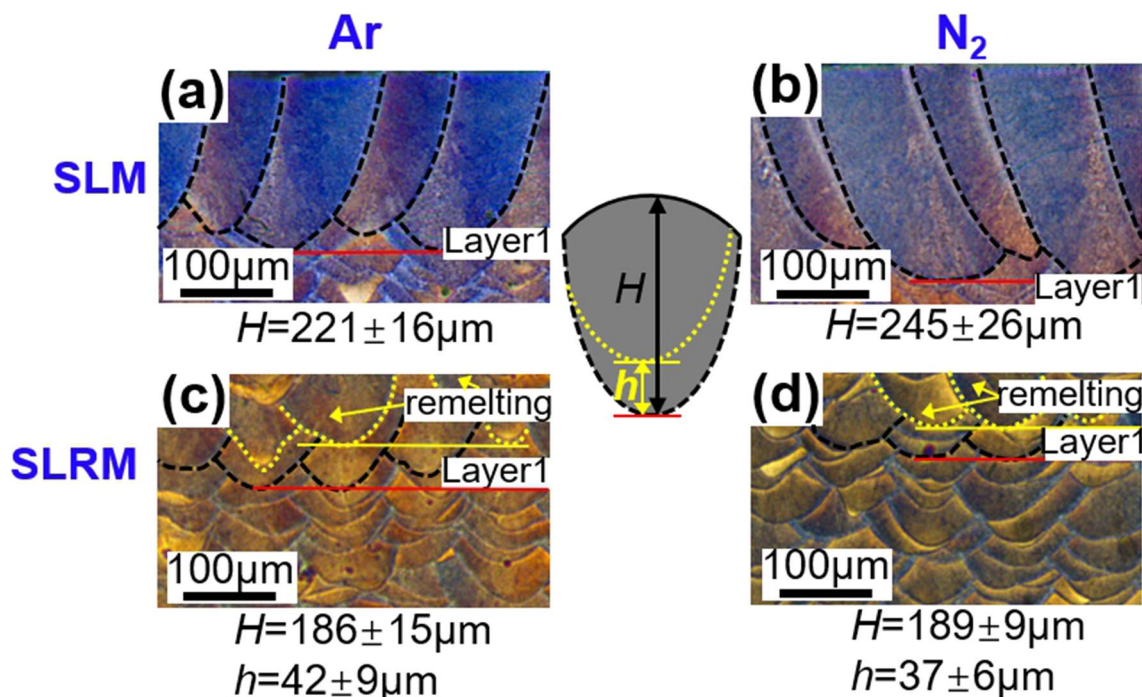


**Fig. 7** Cross section of AlSi10Mg melt pool depth,  $H$  is melt pool depth of single track, and  $h$  is distance of melt pool between previous layer and remelting layer. **a** SLM-Ar build, **b** SLM-N<sub>2</sub> build, **c** SLRM-Ar build, **d** SLRM-N<sub>2</sub> build

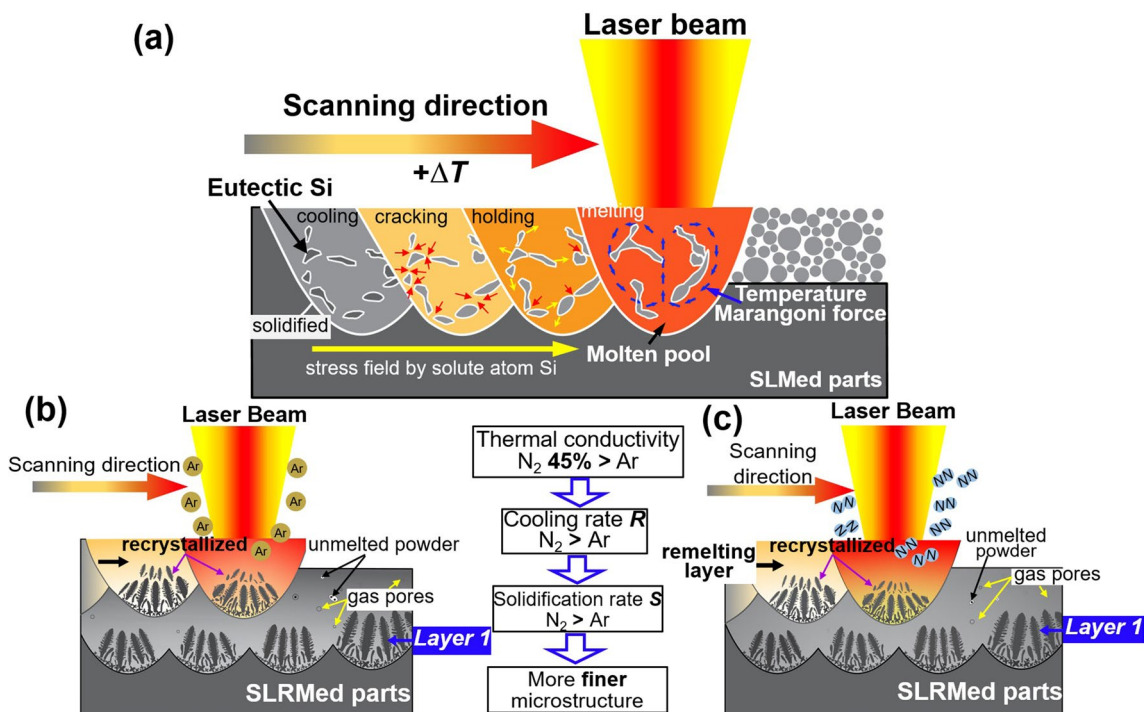


**Fig. 8** a Growth refinement mechanism of eutectic Si in the SLM prepared samples. Strengthening schematic of in situ laser remelting, finer grain growth diagram of remelting and resolidification **b** under argon atmosphere, **c** under nitrogen atmosphere

confirms the above conclusion that the short columnar phase in the crystal grain is the Si phase from the side. However, the distribution of Mg was relatively uniform (Fig. 9c) without enrichment trend, and smaller size of the acicular phase led to the insignificant enrichment of magnesium. Even if there was an enrichment, this phenomenon of fine acicular enrichment scarcely appeared that affected by the uniform Mg solid solution on the  $\alpha$ -Al matrix. Further X-ray energy spectrum analysis showed that the oxygen content and silicon content of the remelted parts were lower than those of the SLM parts. The SLRM-N<sub>2</sub> parts had the lowest oxygen content due to the higher thermal conductivity of nitrogen than that of argon [14]. The content of magnesium in the four batches of samples was equivalent, but with the in-situ laser remelting strategy observing the Si/Mg molar ratio decreased in both argon and nitrogen atmospheres. This also proved that the in situ laser remelting causes silicon to dissolve more in the  $\alpha$ -Al matrix and provides favorable evidence for the difference in tensile properties. That is, supersaturated Si and Mg solid solutions contributed to strengthening the Al matrix.

### 3.3 Mechanical Properties of SLMed and SLRMed Samples

Since different relative density, gas atmosphere [13] and scanning strategies [10] could affect the deformational

behavior, the final experiment was designed to evaluate the mechanical properties of SLM as well as SLRM samples under argon and nitrogen atmosphere. Figure 10a shows the representative stress–strain curves obtained from tensile tests, and the average stress/strain performances are summarized in Table 3. The ultimate tensile strength of the materials remelted under argon and nitrogen atmosphere increased from  $444.85 \pm 8.73$  MPa and  $459.21 \pm 13.77$  MPa to  $489.45 \pm 3.20$  MPa and  $500.14 \pm 5.15$  MPa, respectively, and the elongation after fracture increased from 2.55% and 2.88% to 4.51% and 5.13%. The results show that the tensile strength and elongation of remelted samples are significantly higher compared to those of SLM samples, which is probably attributed to the decrease in porosity [29]. Another reason for the improvement of ductility is thermal residual stress release that occurred in the course of laser remelting. On the other hand, the reduction in grain size of the SLRM sample in this study could further improve the deformability [40, 41], which could be rationalized by the following Hall–Petch formula:

$$\sigma_s = \sigma_0 + K_s \cdot d^{-(1/2)} \quad (2)$$

where symbol  $\sigma_s$  is the yield strength, and  $\sigma_0$  is the frictional resistance of dislocation movement in the single crystal.  $K_s$  is the strength coefficient of the grain boundary barrier, and  $d$  is the size of grain diameter. Obviously, with the grain



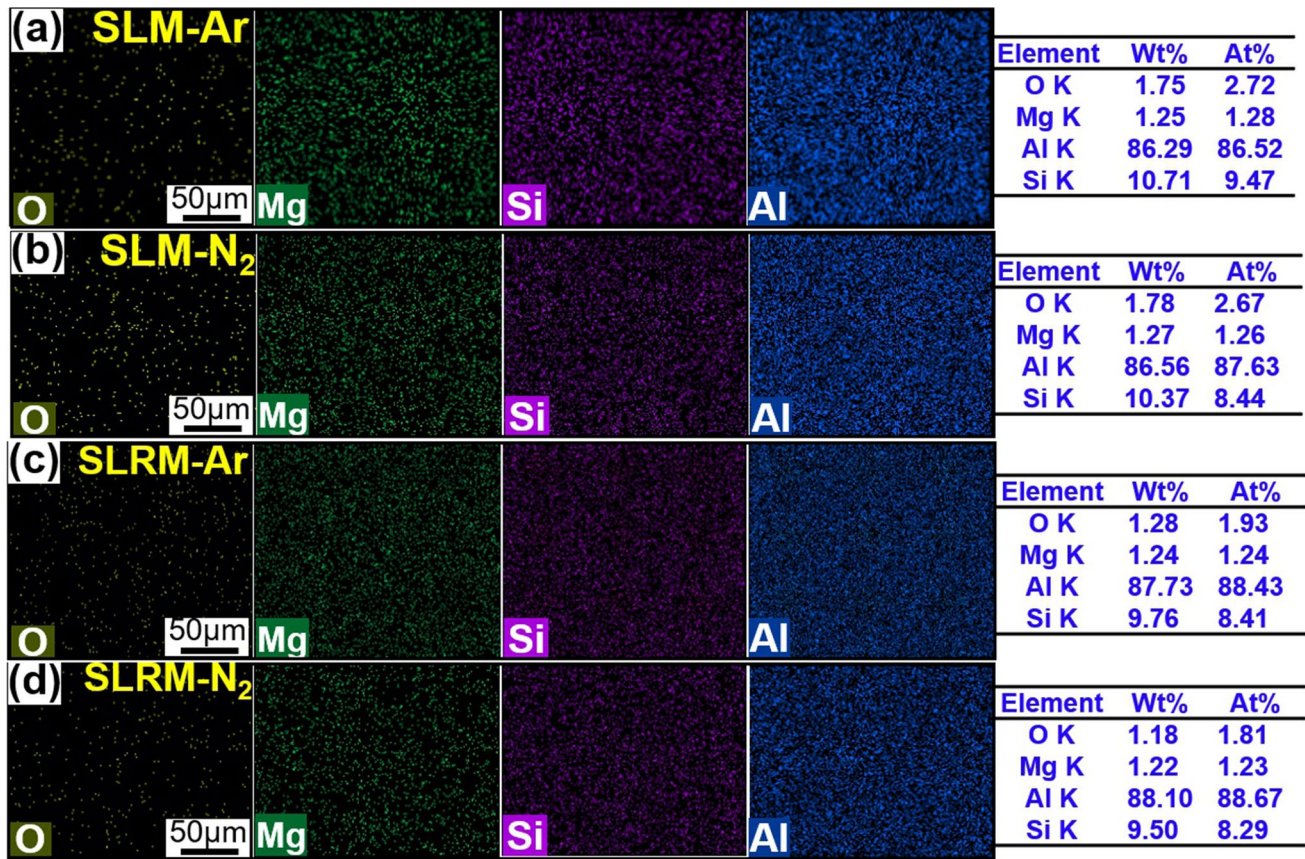


Fig. 9 EDS mapping results of AlSi10Mg alloy: **a** SLM-Ar, **b** SLM-N<sub>2</sub>, **c** SLRM-Ar, **d** SLRM-N<sub>2</sub>

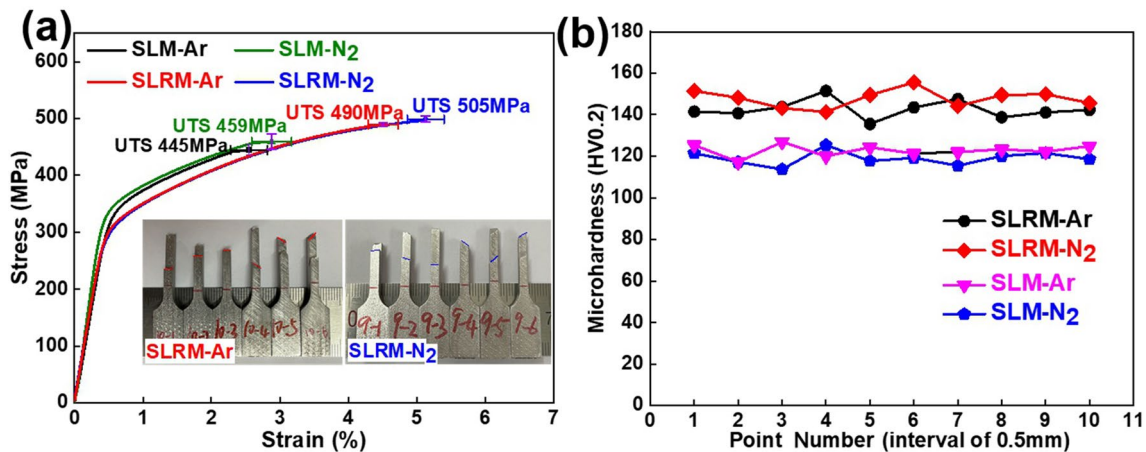


Fig. 10 **a** Tensile stress–strain curve at room temperature of the as-built AlSi10Mg alloy and macroscopic fracture morphology in argon and nitrogen atmosphere; **b** microhardness test of the as-built sample

refining, the amount of grain boundaries increases significantly, resulting in difficulty of dislocation movement, so the plastic deformation resistance and the strength increase. Therefore, the mechanical properties of SLRM-N<sub>2</sub> were superior to that of SLRM-Ar because of finer microstructure

(as elaborated in Sect. 3.2). The yield strength of remelted samples is slightly lower than that of SLM samples. It may be due to laser remelting in situ heat treatment destroying fine-grained structure, precipitation and growth of silicon



**Table 3** Summary of average tensile properties of four batches AlSi10Mg samples fabricated by different process parameters

Samples	Ultimate tensile strength (MPa)	Yield strength (MPa)	Elongation (%)	Elastic modulus (GPa)
SLM-Ar	444.85 ± 8.73	341.49 ± 9.97	2.55 ± 0.27	76.37 ± 10.16
SLM-N <sub>2</sub>	459.21 ± 13.77	346.18 ± 10.45	2.88 ± 0.29	75.84 ± 9.38
SLRM-Ar	489.45 ± 3.20	323.75 ± 2.28	4.51 ± 0.22	72.92 ± 3.99
SLRM-N <sub>2</sub>	500.14 ± 5.15	324.91 ± 4.82	5.13 ± 0.27	70.21 ± 1.44
AM as-built	452 ± 1	264 ± 4	8.6 ± 1.0	Ref. [29]
Gravity Cast-T6	330 ± 13	268 ± 6	3.8 ± 1.5	

The conventional AM as-built and gravity casting samples were also listed

particles, resulting in weakening of solid solution reinforcement and local shear stress release.

The Vickers microhardness results between the SLM samples and the remelted samples are shown in Fig. 10b. The average value of as-built samples under argon atmosphere is  $119.11 \pm 3.33$  HV<sub>0.2</sub>, which is similar to that built under a nitrogen atmosphere with  $122.74 \pm 2.84$  HV<sub>0.2</sub>. This indicates that the sample has uniform microhardness. However, the SLRM samples under nitrogen atmosphere had highest microhardness of  $155.58$  HV<sub>0.2</sub> with an average value of  $148.25 \pm 4.73$  HV<sub>0.2</sub>. Both argon and nitrogen atmospheres result in around 21% microhardness enhancement of the SLRM-processed samples comparing with the SLM samples, which is due to the much finer microstructure produced during in situ laser remelting and resolidification, as shown in Fig. 8b, c. In the laser remelting process, the columnar grains near the top of the original molten pool are remelted and solidified in the same manner as the previous molten pool, thereby reducing the distance between the Si particles and the finer equiaxed grains. In addition, during the SLM additive manufacturing process, the higher cooling rate of the melt pool hindered the precipitation of Si, and part of silicon elements was supersaturated and dissolved in the  $\alpha$ -Al matrix. Moreover, dispersion strengthening phases of needle-like phase and spherical (Mg + Si) cluster zone are also precipitated on the  $\alpha$ -Al matrix, which both can cause lattice distortion and significantly hinder dislocation movement [42]. The supersaturated microstructure in  $\alpha$ -Al matrix improves the strength and microhardness of the AlSi10Mg alloy. The elimination of defects (gas pores, lack of fusion, etc.) also contributes to improve performance.

### 3.4 Fracture Analysis

Figures 11 and 12 show the fracture morphologies of SLMed and SLRMed samples obtained by SEM, respectively. SLMed specimens have similar fracture morphologies: the macroscopic fracture morphology, as shown in Fig. 11a, d, both showed rough and irregular fracture with obvious microcracks and cavities. From the high magnification images of the SLMed sample (Fig. 11b, e), a number

of round holes could be seen. These round holes are mainly derived from the powder and hydrogen absorption caused by moisture and oxide inclusions [26]. On the microscopic fracture morphology, tensile fractures of the SLMed specimens are all distributed with obvious stepped and lacerated cleavage steps as well as tiny dimples, which belong to quasi-cleavage fracture. No cleavage morphology was observed [43], the cleavage structure also tended to generate relatively brittle fracturing. However, tiny shallow dimples and columnar grains corresponding to ductile fracture were found on the fracture surface (arrows in Fig. 11c, f). The cavities perpendicular to the construction direction are mainly derived from lack of fusion between adjacent tracks and large oxide particles that were poor wetting with the  $\alpha$ -Al matrix [44]. The visible cleavage fracture structure was the result of the combined effect of the small anisotropic columnar grains and the residual stress generated by the SLM process. The shape of the hole defect became flat at the bottom after transverse stretching. Cracks originate from defects such as irregular holes which will form large stress concentrations during the tensile process and first reach the yield strength limit leading to produce cracks, and subsequently, rapidly expand along the close-packed plane of the crystal. These defects will become the source of cracks that lead to low tensile strength as well as low plasticity, as shown in Fig. 11e. The edge of holes on the fracture surface of the SLM-N<sub>2</sub> sample was relatively bright without small shear dimples, which indicates that the fracture of the sample around the hole is also brittle fracture. While there are also a number of circular shallow dimples (Fig. 11f) on the tensile fracture, revealing that the material still had a certain plasticity. Except for defects, SLMed samples failed along the rhombic and dendritic network (see Fig. 6b, e). This fracture was most likely propagated from the hatch spacing overlaps, where the density of the brittle silicon phase was higher than in other areas. Due to the high hardness and low plasticity of the silicon-rich network, it became a failure point under tensile load [4]. Combining the samples with low plastic properties in Table 3, it can be found that many cleavage surfaces reveal brittle fracture characteristics with low elongation.

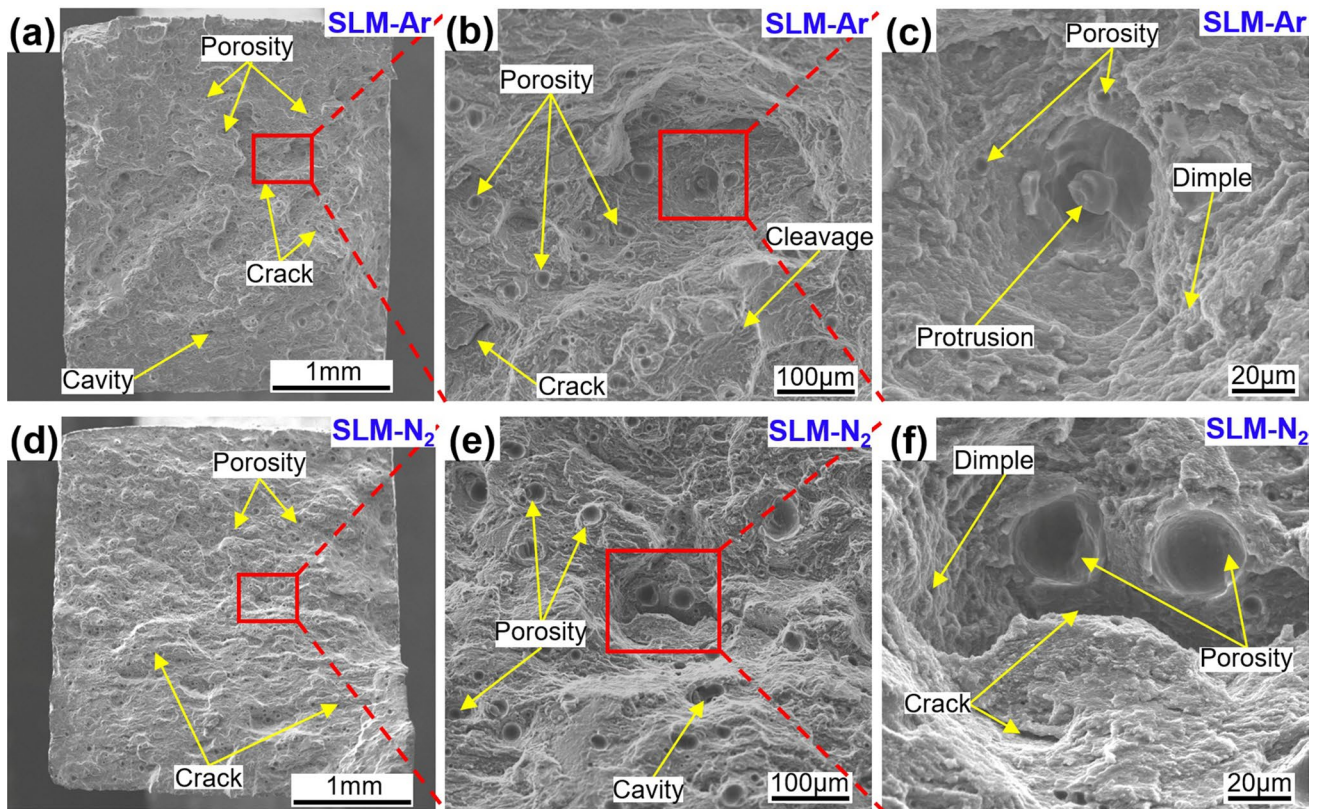


**Fig. 11** Fracture morphologies of AlSi10Mg alloy fabricated by SLM: **a–c** in the argon atmosphere, **d–f** in the nitrogen atmosphere

Figure 12 shows the fracture morphology of the SLRM tensile specimens. However, combined with metallographic images, few shrinkage cavities and unmelted powders were found in the SLRMed sample fracture. The reduction of pores will increase the tensile strength and elongation of the specimen, which was consistent with the tensile test. Dimples were observed in all SLRMed specimens, and the plasticity of the tested specimens was higher than that in prior SLM [29, 45]. Compared with conventional SLMed samples, the propagation of crack on the boundary of molten pool more occurs through intergranular failure in SLRMed samples, and the existence of dimples is consistent with the larger plastic strain in tension. Figure 12e shows many large and deep dimples on the fracture surface, and some protrusions of different sizes and shapes are also observed in Fig. 12f, which related to the heat treatment by in situ laser remelting. It should be noticed that the dimples in the SLRM-N<sub>2</sub> samples are deeper than the SLRM-Ar samples, which could be explained by the different thermal conductivity of two gas leading to different grain growth rate during the SLM process. The in situ laser remelting heat treatment encouraged grain growth, Si phase precipitation and residual stress release, all of which cause the elongation after fracture increases comparing to the SLM sample.

## 4 Conclusions

The results showed that the decrease in the strength and deformation properties of the SLMed material is related to pore discontinuity (relative density), whereas the pores play a role of stress concentrators and crack initiation. A comprehensive study was conducted on microstructures and properties of AlSi10Mg samples prepared by SLM remelting process under argon and nitrogen atmosphere with those obtained from SLM processing run. The main conclusions are drawn as follows:

1. Due to a good metallurgical bonding between adjacent molten pools and the formation of shallower molten pools, the in situ laser remelting can effectively enhance the relative density (99.5%) at the cost of increasing production time. Compared with samples without remelting treatment, the laser remelted samples clearly showed a finer microstructure. Rapid remelting and resolidification can explain the refinement and uniform distribution of the microstructures.
2. Parts produced by SLM remelting performed significantly enhanced properties compared with those produced by SLM both in argon and nitrogen atmospheres, and the performance of nitrogen was better



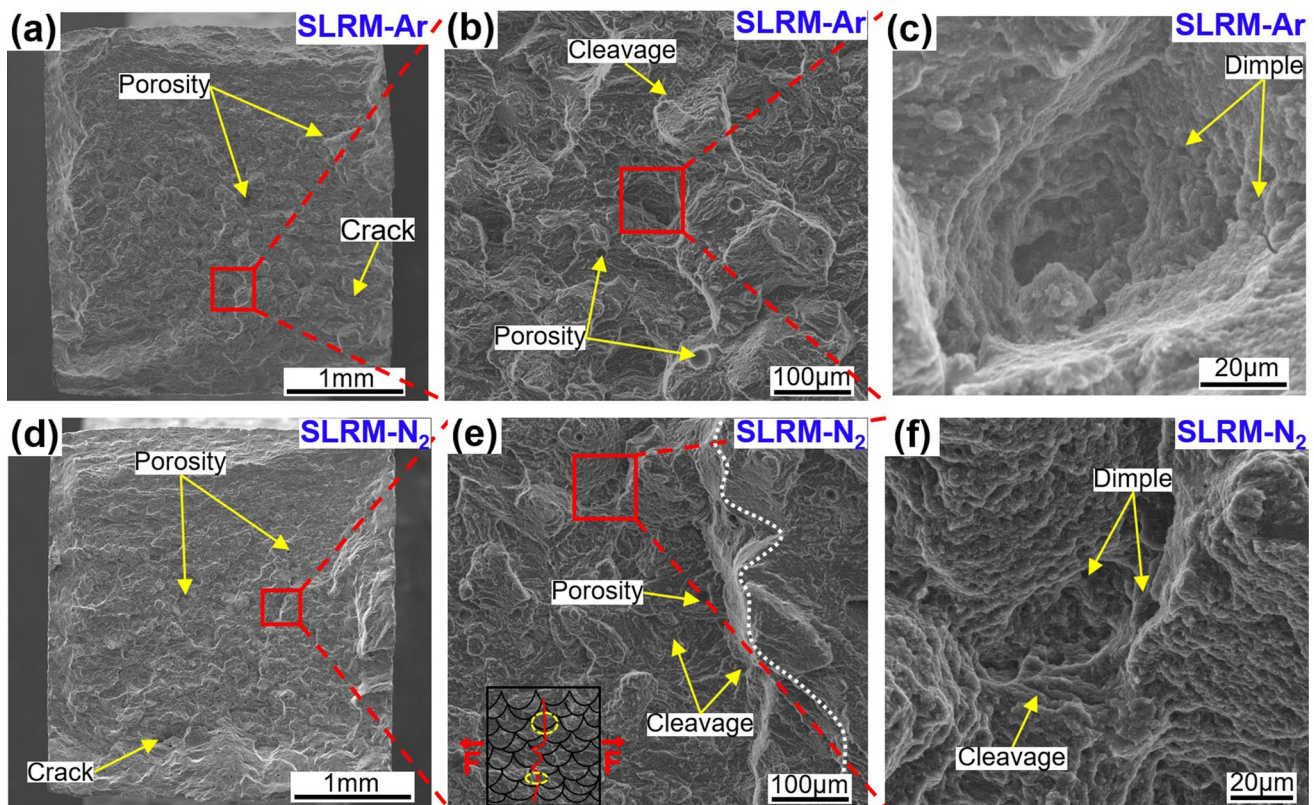


**Fig. 12** Fracture morphologies of AlSi10Mg alloy fabricated by SLRM: **a–c** in the argon atmosphere, **d–f** in the nitrogen atmosphere

than that of argon. The tensile tests show that ultimate tensile strength of the material with laser remelting is increased 12.6% and twice the elongation at break, but the yield strength decreases slightly from  $341.49 \pm 9.97$  to  $324.91 \pm 4.82$  MPa. In addition, the micro-mechanism of fracture is of ductile in all SLRMed conditions, with more and shallower dimples than SLM.

3. Compared with the SLMed relatively coarse AlSi10Mg powder, the combined effects of finer microstructure, lower porosity and solution strengthening due to laser remelting enhanced around 30  $HV_{0.2}$  microhardness comparing to the AlSi10Mg alloy built via SLM under nitrogen atmosphere.

**Acknowledgements** This work was financially supported by the NSFC-Guangdong Joint Foundation Key Project (No. U2001218), the Key-Area Research and Development Program of Guangdong Province (No. 2020B090924002), the National Natural Science Foundation of China (Nos. 51875215, 81772428), the Ministry of Education Key Laboratory of High-Efficiency Near-Net-Shape Forming Technology and Equipment for Metal Materials Open Fund (No. 2019005)

## Declarations

**Conflict of interest** The authors declare that they have no known competing financial interests or personal relationships that could have appeared to influence the work reported in this paper.

## References

- [1] J.H. Martin, B.D. Yahata, J.M. Hundley, J.A. Mayer, T.A. Schaedler, T.M. Pollock, *Nature* **549**, 365 (2017)
- [2] S. Dadbakhsh, R. Mertens, L. Hao, J. Van Humbeeck, J.P. Kruth, *Adv. Eng. Mater.* **21**, 1801244 (2019)
- [3] K.G. Prashanth, R. Damodaram, S. Scudino, Z. Wang, K. Prasad Rao, J. Eckert, *Mater. Des.* **57**, 632 (2014).
- [4] U. Tradowsky, J. White, R.M. Ward, N. Read, W. Reimers, M.M. Attallah, *Mater. Des.* **105**, 212 (2016)
- [5] N.T. Aboulkhair, N.M. Everitt, I. Ashcroft, C. Tuck, *Addit. Manuf.* **1–4**, 77 (2014)
- [6] L.N. Carter, C. Martin, P.J. Withers, M.M. Attallah, *J. Alloys Compd.* **615** (2014).
- [7] N. Read, W. Wang, K. Essa, M.M. Attallah, *Mater. Des.* **65**, 417 (2015)



- [8] H.H. Wu, J.F. Li, Z.Y. Wei, P. Wei, *Rapid Prototyp. J.* **26**, 871 (2020)
- [9] L. Thijs, K. Kempen, J.-P. Kruth, J. Van Humbeeck, *Acta Mater.* **61**, 1809 (2013)
- [10] E. Yasa, J. Deckers, J.P. Kruth, *Rapid Prototyp. J.* **17**, 312 (2011)
- [11] A.G. Demir, B. Previtali, *Int. J. Adv. Manuf. Technol.* **93**, 2697 (2017)
- [12] J. Vaithilingam, R.D. Goodridge, R.J.M. Hague, S.D.R. Christie, S. Edmondson, *J. Mater. Process. Technol.* **232**, 1 (2016)
- [13] S. Traore, M. Schneider, I. Koutiri, F. Coste, R. Fabbro, C. Charpentier, P. Lefebvre, P. Peyre, *J. Mater. Process. Technol.* **288**, 116851 (2021).
- [14] X.J. Wang, L.C. Zhang, M.H. Fang, T.B. Sercombe, *Mater. Sci. Eng. A* **597**, 370 (2014)
- [15] M.A. Balbaa, A. Ghasemi, E. Fereiduni, M.A. Elbestawi, S.D. Jadhav, J.P. Kruth, *Addit. Manuf.* **37**, 101630 (2021).
- [16] ASTM B213–17, Standard Test Methods for Flow Rate of Metal Powders Using the Hall Flowmeter Funnel, ASTM International, ASTM International, West Conshohocken, PA (2017).
- [17] ISO 3522:2007, Specifics the Chemical Composition Limits for Aluminium Casting Alloys and Mechanical Properties of Separately Cast Test Bars for These Alloys (2007).
- [18] Y. Bai, Y. Yang, Z. Xiao, M. Zhang, D. Wang, *Mater. Des.* **140**, 257 (2018)
- [19] A.B. Spierings, M. Schneider, R. Eggenberger, *Rapid Prototyp. J.* **17**, 380 (2011)
- [20] ASTM E112-13, Standard Test Methods for Determining Average Grain Size. ASTM International, West Conshohocken, PA (2013).
- [21] ISO 6892-1:2019, Metallic Materials—Tensile Testing—Part 1: Method of Test at Room Temperature (2019).
- [22] G.E. Jauncey, *Proc. Natl. Acad. Sci. USA* **10**, 57 (1924)
- [23] D. Carluccio, M.J. Birmingham, Y. Zhang, D.H. StJohn, K. Yang, P.A. Rometsch, X. Wu, M.S. Dargusch, *J. Manuf. Processes* **35**, 715 (2018)
- [24] T. Gustmann, H. Schwab, U. Kuhn, S. Pauly, *Mater. Des.* **153**, 129 (2018)
- [25] J. Chen, W. Hou, X. Wang, S. Chu, Z. Yang, *Chin. J. Aeronaut.* **33**, 2043 (2020)
- [26] C. Weingarten, D. Buchbinder, N. Pirch, W. Meiners, K. Wissenbach, R. Poprawe, *J. Mater. Process. Technol.* **221**, 112 (2015)
- [27] E. Sjölander, S. Seifeddine, *J. Mater. Process. Technol.* **210**, 1249 (2010)
- [28] C.A. Biffi, J. Fiocchi, A. Tuissi, *J. Alloys Compd.* **755**, 100 (2018)
- [29] L. Girelli, M. Tocci, M. Gelfi, A. Pola, *Mater. Sci. Eng. A* **739**, 317 (2019)
- [30] Q. Yan, B. Song, Y.S. Shi, *J. Mater. Sci. Technol.* **41**, 199 (2020)
- [31] Q.Y. Tan, J.Q. Zhang, N. Mo, Z.Q. Fan, Y. Yin, M. Birmingham, Y.G. Liu, H. Huang, M.X. Zhang, *Addit. Manuf.* **32**, 101034 (2020).
- [32] N. Kang, P. Coddet, L. Dembinski, H. Liao, C. Coddet, *J. Alloys Compd.* **691**, 316 (2017)
- [33] L.F. Wang, J. Sun, X.L. Yu, Y. Shi, X.G. Zhu, L.Y. Cheng, H.H. Liang, B. Yan, L.J. Guo, *Mater. Sci. Eng. A* **734**, 299 (2018)
- [34] T. Kurzynowski, K. Gruber, W. Stopyra, B. Kuźnicka, E. Chlebus, *Mater. Sci. Eng. A* **718**, 64 (2018)
- [35] W. Kurz, B. Giovanola, R. Trivedi, *Acta Metall.* **34**, 823 (1986)
- [36] M. Zimmermann, M. Carrard, W. Kurz, *Acta Metall.* **37**, 3305 (1989)
- [37] G. Vastola, G. Zhang, Q.X. Pei, Y.W. Zhang, *Addit. Manuf.* **7**, 57 (2015)
- [38] W. Kurz, C. Bezençon, M. Gäumann, *Sci. Technol. Adv. Mater.* **2**, 185 (2001)
- [39] F.M. Faubert, G.S. Springer, *J. Chem. Phys.* **57**, 2333 (1972)
- [40] D. Gu, H. Wang, G. Zhang, *Metall. Mater. Trans. A* **45**, 464 (2013)
- [41] C. Gao, Z. Wang, Z. Xiao, D. You, K. Wong, A.H. Akbarzadeh, *J. Mater. Process. Technol.* **281**, 116618 (2020).
- [42] N. Takata, M. Liu, H. Kodaira, A. Suzuki, M. Kobashi, *Addit. Manuf.* **33**, 101152 (2020).
- [43] J. Suryawanshi, K.G. Prashanth, S. Scudino, J. Eckert, O. Prakash, U. Ramamurty, *Acta Mater.* **115**, 285 (2016)
- [44] T.H. Park, M.S. Baek, H. Hyer, Y. Sohn, K.A. Lee, *Mater. Character.* **176**, 111113 (2021).
- [45] M.J. Paul, Q. Liu, J.P. Best, X. Li, J.J. Kruzic, U. Ramamurty, B. Gludovatz, *Acta Mater.* **211**, 116869 (2021).